Nuclear Materials and Energy 43 (2025) 101916

Contents lists available at ScienceDirect

Nuclear Materials and Energy

journal homepage: www.elsevier.com/locate/nme

X-point radiation: From discovery to potential application in a future reactor

M. Bernert [a,*], T.O.S.J. Bosman [b,c], T. Lunt [a], O. Pan [a], B. Sieglin [a], U. Stroth [a,d], A. Kallenbach [a], S. Wiesen [b], M. Wischmeier [a], G. Birkenmeier [a,d], M. Cavedon [e], B. Lipschultz [f], C. Lowry [g], N. Fedorczak [h], P. Fox [g], M. Lennholm [g], H. Sun [g], P. Jacquet [g], K. Kirov [g], N. Vianello [i], D. Brida [a], S. Henderson [g], P. David [a], R. Dux [a], R.M. McDermott [a], H. Reimerdes [j], C. Theiler [j], M. Komm [k], O. Février [j], U. Sheikh [j], S. Menmuir [g], J.T.W. Koenders [b,c], L. Ceelen [b,c], M.G. Dunne [a], O. Kudlacek [a], F. Reimold [a], the EUROfusion Tokamak Exploitation Team[1], the TCV team[2], the WEST team[3], the JET Contributors[4], the ASDEX Upgrade team[5]

[a] Max Planck Institute for Plasma Physics, Boltzmannstr. 2, 85748 Garching, Germany
[b] DIFFER - Dutch Institute for Fundamental Energy Research, De Zaale 20, 5612 AJ Eindhoven, Netherlands
[c] Department of Mechanical Engineering, CST Group, Eindhoven University of Technology, Eindhoven, Netherlands
[d] TUM School of Natural Sciences, Physics Department, Technical University of Munich, 85748 Garching, Germany
[e] Dipartimento di Fisica "G. Occhialini", Università di Milano-Bicocca, Milano, Italy
[f] University of York, York Plasma Institute, Heslington, York, YO10 5DD, United Kingdom
[g] UKAEA Culham, Culham Science Center, Abingdon, Oxon OX14 3DB, United Kingdom of Great Britain and Northern Ireland
[h] CEA, IRFM, F-13108 Saint-Paul Lez Durance, France
[i] Consorzio RFX, Corso Stati Uniti 4, 35127 Padova, Italy
[j] EPFL, Swiss Plasma Center (SPC), CH, 1015, Lausanne, Switzerland
[k] Institute of Plasma Physics AS CR, v.v.i., Za Slovankou 3, 182 00 Prague 8, Czech Republic

ARTICLE INFO

Keywords:
X-point radiation
Tokamak power exhaust
Impurity seeding
ELM suppression
Divertor detachment
Radiative Scenarios

ABSTRACT

Power exhaust is a crucial issue for future fusion reactors. Divertor detachment and the required power dissipation fractions of about 95% are foreseen to be achieved by impurity seeding. In a tokamak, at high seeding levels the radiation often concentrates in a small region inside the confined plasma near the X-point. In early observations the so-called X-point radiator (XPR) often led to back-transitions to L-mode or disruptions. In metal tokamaks or with higher available heating power, these regimes can be stabilized and are now established on AUG, JET, TCV, KSTAR and WEST.

The XPR is a cold, dense plasma inside the confined region in the vicinity of the X-point, that breaks the paradigm of poloidal symmetry of density and temperature on closed flux surfaces. On AUG, the poloidal extent of the XPR is a few centimeters and it is observed up to 15 cm above the X-point. The long connection length in this region and the access of neutral particles from the divertor region facilitate the creation of the XPR, as predicted by an analytical model. Numerical simulations with SOLPS-ITER match the observations at AUG and TCV and allow predictions towards a power plant, where a lower impurity concentration is required to trigger an XPR. Since the XPR greatly reduces power and particle fluxes to the targets, simpler and more efficient divertor concepts, such as the compact radiative divertor, can be envisaged for future devices. A scenario with an XPR, however, comes at the cost of an increased impurity concentration and a potential reduction in confinement, which has to be further quantified.

* Corresponding author.
E-mail address: matthias.bernert@ipp.mpg.de (M. Bernert).

[1] See the author list of E. Joffrin et al 2024 Nucl. Fusion in press https://doi.org/10.1088/1741-4326/ad2be4.
[2] See the author list of H. Reimerdes et al 2022 Nucl. Fusion 62 042018.
[3] See http://west.cea.fr/WESTteam.
[4] See the author list of C.F. Maggi 2024 Nucl. Fusion in press https://doi.org/10.1088/1741-4326/ad3e16.
[5] See the author list of H. Zohm et al 2024 Nucl. Fusion in press https://doi.org/10.1088/1741-4326/ad249d

https://doi.org/10.1016/j.nme.2025.101916
Received 5 July 2024; Received in revised form 12 February 2025; Accepted 3 March 2025
Available online 25 March 2025

The XPR location can be well detected by various diagnostics, enabling responsive real-time control, even through large transients like an LH transition. The active control helped to access a new regime of ELM suppression at AUG, which is now also observed at TCV and JET.

The observation of the XPR on multiple tokamaks, the demonstration of its active control, and the emergence of theoretical models that scale favourably towards fusion reactors have opened up a new phase of advanced power exhaust research.

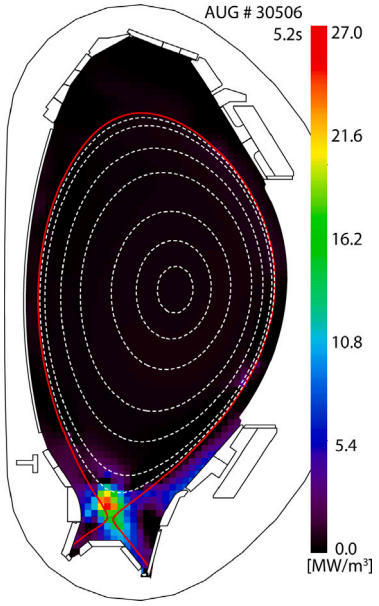

Fig. 1. Tomographic reconstruction of the total radiation emitted in AUG #30506. The XPR is clearly visible above the X-point, the dashed lines indicate the flux surfaces inside the confined plasma, the red line is the separatrix forming the magnetic X-point. (For a coloured version of this figure, the reader is referred to the web version of this article.).
Source: Figure adapted from [4].

1. Introduction: What is an X-point radiator?

In recent years, X-point radiation was observed in ASDEX Upgrade (AUG) [1–3], JET [4,5], TCV [6–8], KSTAR [9] and WEST [10–12]. The X-point radiator (XPR) stands out as a region of intense radiation (1–30 MW/m^3, see Fig. 1), low electron temperatures (1–2 eV) and high density ($> 3 \cdot 10^{20}\,/m^3$) inside the confined region at or above the X-point.

A radiation condensation, triggered by the temperature dependence of impurity radiation (see Section 3), leads to this strongly localized cooling. With the presence of an XPR, parallel temperature gradients exist inside the confined region, which breaks the usual assumption of constant density and temperature on flux surfaces. With such gradients, the XPR region acts as a virtual limiter, radiating a significant fraction of the total heating power, usually accompanied by full detachment, and ensuring the high dissipated power fraction as required for a future reactor [13].

An XPR is usually initialized by strong impurity seeding, which is injected to increase the power dissipation. It has been obtained by seeding of nitrogen, neon, argon and krypton [4] or combinations thereof, but can also be created by the sole injection of deuterium [8,9,14]. The latter case relies most likely on intrinsic impurities to be sufficient to trigger the radiation condensation. With higher seeding levels (or fuelling), the XPR moves further inside the plasma and is, at AUG, observed up to 15 cm above the X-point, corresponding to $\rho_{pol} \geq 0.985$ or less than 10 mm inside the separatrix if mapped to the outer midplane.

The XPR is likely the same phenomenon as a MARFE [15], which is also triggered by a radiation condensation and creates a highly radiating zone at the edge of the plasma. A MARFE is typically observed close to the X-point or at the high field side in high density plasmas without additional impurity seeding and usually initiates a disruption [16]. The work by Sieglin et al. [14] shows that a MARFE and an XPR might be the same phenomenon. The term *"X-point radiation"* was introduced to distinguish a stable operational regime from the MARFE occurrence, which most often ends in a disruption. Therefore, we use here the distinction adapted from [17]:

- XPR: A radiating region that sits stably and actively controllable close to the X-point, typically initiated by impurity seeding.
- MARFE: A meta-stable scenario in which the radiator moves upwards and triggers a disruption, typically initiated by strong fuelling.

In Section 2, we first review earlier observations (1980s to 2010) of more or less stable radiation at the X-point, and discuss why these scenarios were not further pursued. In Section 3 we discuss the existing analytical and numerical models for XPRs. In Section 4, the observations in current fusion experiments are summarized, focusing on the latest experiments at ASDEX Upgrade (Section 4.1) and JET (Section 4.2), the latter including experiments in deuterium–tritium plasmas. The existence of XPRs in future tokamaks like ITER and DEMO is investigated in 5.1, discussing the impurity requirements and the potential impact on the confinement. We show potential applications that utilize the features of the XPR to ease the construction and operation of future tokamaks in Section 5.4 & 5.5. The paper is summarized in Section 6, highlighting open questions for further research on XPRs.

2. Earlier observation of radiation inside of the X-point

MARFEs are a commonly observed phenomenon in tokamak operation and were in the 1980's already well understood, see Lipschultz et al. [15]. MARFEs are usually observed at high densities, occurring at similar densities as detachment of the divertor, and might also be correlated with the latter. However, MARFEs were observed to initiate a disruption (e.g. [16,18,19]), usually proceeded by an upward movement of the MARFE. This also determines the density limit in many tokamaks [14]. A few cases are reported where the MARFE onset was actively [20] or iteratively [21] controlled and the upward movement avoided, e.g. by additional heating power or reduced gas fuelling.

In contrast to the disruptive MARFE phenomenon, there are also reports of a radiating region existing inside the confined plasma for at least several energy confinement times. These were typically achieved with external impurity seeding. For JET with carbon plasma facing surfaces, this was first achieved with nitrogen seeding [22] and later also with neon and argon seeding [23].

For AUG with carbon tiles, the completely detached H-mode (CDH) [24] featured intense radiation at the X-point with either nitrogen, argon or neon seeding (the latter applying active control) [25–27]. These experiments focused on the radiating mantle inside/along the separatrix and did not identify a condensation of the radiation close to the X-point, despite the high emissivity in this region. This was believed to be an effect of the limited spatial resolution of the diagnostics.

The investigations of the CDH mode at AUG were influenced by the radiation improved mode (RI-mode) discovered at TEXTOR [28]. As TEXTOR is a circular device, which does not have an X-point, an XPR

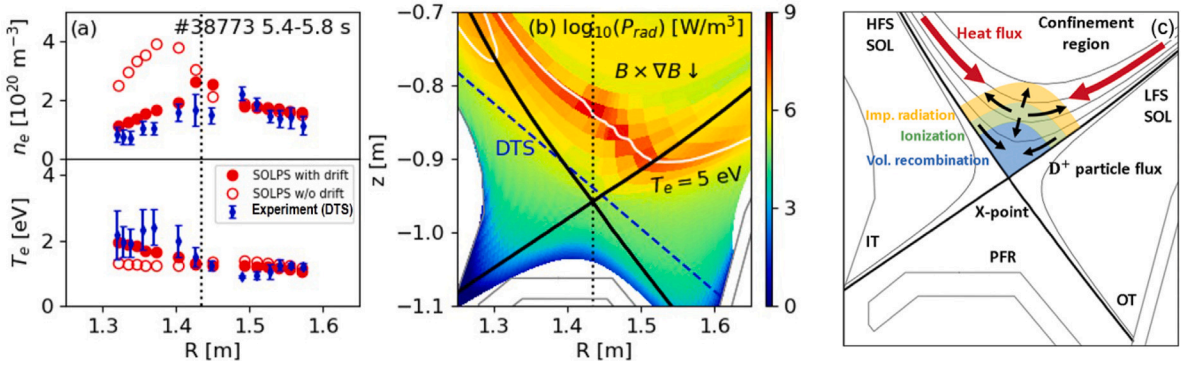

Fig. 2. SOLPS-ITER simulations (with drifts activated and Nitrogen seeding) based on AUG discharge # 38773 at 3.5 s. (a) Match of experimental measurements of electron density and temperature by Divertor Thomson Scattering (DTS) with simulations with and without drifts at higher seeding levels, corresponding to the time point of 5.4–5.8 s; (b) simulated radiation distribution and electron temperature contour for the matched case with drifts; (c) sketch of XPR structure (without drifts) with the cold core (vol. recombination) surrounded by an ionization region and radiating region. (For a coloured version of this figure, the reader is referred to the web version of this article.).
Source: Figures adapted from [35].

cannot be present. The overall radiation was increased in a poloidally symmetric radiation belt and confinement improvement was observed, while remaining in an L-mode like plasma. This regime has some similarity with the ELM suppression observed with the XPR, further discussed in Section 4.1.2.

Increased radiation inside the X-point was also observed at Alcator C-Mod with Ne or CD_4 seeding [29], and TCV with Ne seeding [30] or without extrinsic seeding, for example at JT60-U [31].

All of the above references mention the radiation inside the confined plasma. In some cases (e.g. JET and AUG), this is reported as a viable exhaust regime for a reactor, featuring small ELMs, while in other cases (e.g. TCV, Alcator C-Mod and JT60-U) the regimes were disregarded as they were unstable and led to disruptions. All references report a reduced confinement or reduced core electron temperature, and some mention an increased core impurity concentration or a loss of neutral compression of the divertor. These drawbacks overall led to a loss of interest in such regimes, since the main priority at that time was the development of ITER scenarios with a maximized energy confinement. Partial detachment was expected to be sufficient for divertor protection at ITER, while not implying a reduction in confinement [32]. Therefore, partial detachment became the operational design point, radiation from the confined region should be minimized to limit the effect on the core (Z_{eff}, pedestal cooling) [33]. Additionally, the change of the JET operational structure [34], shutdown of TEXTOR and other changes in the community lead to less attention being paid to those regimes.

In contrast, today the focus is shifting towards reactor operational scenarios, where a dissipated power fraction of $\geq 95\%$ [13] and the absence of large ELMs are required [36]. The detailed investigations on the expected heat load density in a reactor (e.g. [37]) furthermore enforced the need of fully detached divertor operation in a reactor and the requirement to actively control such a state. In metal-walled machines impurity seeding becomes inevitable to handle the power exhaust [38]. In this context, regimes with higher radiation and radiation from inside the confined region, such as the XPR, are necessary.

3. Existing analytic and numerical models

It was only possible to identify that the XPR is located inside the confined plasma by combining experimental observations [39] and SOLPS simulations [1] at AUG. The early modelling was based on SOLPS 5.0 without drifts and was only possible with an "unconventional assumption on the perpendicular transport" [1], i.e. by increasing the transport coefficients close to the X-point by up to a factor of 10. With SOLPS-ITER [40], it is possible to reproduce the XPR with drifts activated [35,41], achieving a more stable numerical solution and investigating the impact of drifts on the XPR. Also for KSTAR [9] and TCV [42] the experimental observations of an XPR can be reproduced by SOLPS-ITER.

Fig. 2 shows the match of the SOLPS-ITER modelling with experiments and a sketch of the structure that can be deduced from the modelling: The cold core of the XPR, with electron temperatures below 5 eV and significant volumetric recombination, is surrounded by a layer of high ionization rates. This ionizing layer is fed by neutral particles from the cold core, and its high electron density leads to a radially inward diffusion into the radiating layer, increasing the density, and thus, radiative losses there. The radiating layer, dominated by the seed impurity radiation, dissipates most of the heat flux arriving from the upstream region.

An analytic model for the XPR, developed by Stroth et al. [17], helps to further understand the dominant parameters to create and maintain an XPR inside closed field lines. The model is based on a power balance of conducted power from the upstream location with the losses in the XPR region, consisting of ionization, charge-exchange and radiative losses. The power balance results in two stable operational points (one high temperature (*ht*) and one low temperature (*lt*) solution) as well as one unstable solution. The presence of impurity radiation is necessary, but the absolute magnitude of the radiated power by the impurity, and thus impurity concentration, does, to first order, not matter for the existence of the two operational points. The *ht* solution reflects the standard operation with a hot X-point at similar temperatures to the upstream position. The *lt* solution is interpreted as the XPR after a radiation condensation occurs. The temperature of this operational point mainly depends on the dominant impurity and its radiation characteristics (in the corona approximation about 1 eV for carbon, 1.5 eV for nitrogen and 2 eV for argon).

Depending on the parameters (e.g. a high neutral density), the *ht* solution can vanish in the model. This is interpreted as the access to the *lt* solution and, thus, the triggering of an XPR. The access condition can be formulated as:

$$X_A \propto \frac{R_0^2 q_s^2 f_{exp}}{a} \frac{n_u n_0}{T_u^{5/2}}$$

[17], X_A being the access parameter, which has to be exceeded, R_0 the major radius, $q_s = B_\phi a/(B_\theta R_0)$ the safety factor for a circular plasma, f_{exp} the averaged flux expansion of the XPR region, a the minor radius, n_u and T_u the upstream kinetic parameters and n_0 the neutral density at the X-point. Following this model, the main parameters for the access to an XPR are a high flux expansion (or a long connection length to the midplane), a high neutral density at the X-point and the upstream parameters, n_e & T_e. This also highlights why an XPR is triggered at the X-point: the flux expansion is highest and the neutral particles can easily enter from the private flux region.

At temperatures below 1.5 eV, the deuterium recombination rate increases strongly, therefore a pressure reduction is predicted, which leads to an inward movement of the pressure hole. This is interpreted as the unstable MARFE, which initiates subsequently a disruption [17]. In this way, the model describes the operational space between stable XPRs and unstable MARFEs. For an XPR triggered by carbon, which cools down to about 1 eV, stable XPRs can exist only at low density and heating power, while for nitrogen at about 1.5 eV the operational space is significantly broader (see Figure 9 in [17]).

With the implementation of neutral particle physics and impurity models in advanced simulation frameworks, XPRs can also be reproduced by those codes. This allows, for example, turbulence investigations in the XPR regime by Grillix [43] or MHD and pedestal stability calculations applying JOREK. SOLPS-ITER simulations of the XPR focus more and more on large scale tokamaks [44,45].

4. Observations of XPRs in current tokamaks

Stable radiation at the X-point is observed today in many tokamaks and also in the stellarator W7-X. It is typically induced by strong impurity seeding of either nitrogen, neon, argon or krypton, but can also be initiated by pure deuterium fuelling without being MARFE unstable (see Section 1). Here, we will report the main observations on the different devices, with special emphasis on ASDEX Upgrade (AUG), where the XPR was rediscovered as a stable regime and extensively studied due to its beneficial properties in a metal wall machine, and JET, the biggest tokamak to operate with an XPR, including experiments with deuterium–tritium plasmas.

4.1. ASDEX upgrade

In the 2012 AUG experimental campaign, the presence of localized radiation at the X-point was clearly observed in plasma discharges featuring nitrogen seeding [1]. Later it was also observed with argon seeding [3]. Neon and krypton seeding might also initiate an XPR, but due to their transport and radiation properties, and their impact on the H-mode operation, these seed impurities lead to a radiative collapse of the plasma [4]. With the onset of the XPR, the outer divertor is in pronounced detachment [46], while the inner divertor is already detached under standard conditions. From the volume of the XPR, about 40% of the heating power is radiated, while the entire radiated power fraction is in the range of 80–100%. XPRs are observed with nitrogen seeding in L- & H-modes and can be created in the full operational range of AUG at high density ($P_{heat} = 1.7 - 26$ MW, $I_P = 0.8 - 1.2$ MA, $B_T = 1.8$ & 2.5 T, $f_{GW} \geq 0.7$) [7].

The XPR is initiated close to the X-point and observed to move with increased seeding rate inside the plasma up to 15 cm above the X-point. The movement and its control are further described in the next section. With a location higher than about 7 cm, ELM suppression is observed. This is further discussed in 4.1.2.

4.1.1. Movement & control

After the XPR is initiated, it moves further inside the confined plasma with increasing seeding/fuelling and is observed to exist stably up to 15 cm above the X-point. A location inside the confined plasma can be reproduced by SOLPS modelling (see Section 3) and the trend is reproduced, however, the full movement is not described yet. The location can be tracked in two dimensions using AXUV diodes [47]. For favourable drift direction (ion diamagnetic drift pointing to the active X-point), the XPR moves along a crescent shape upwards first towards the low field side and above ~5 cm turns in direction towards the high field side. When reducing the seeding (or increasing heating power), the XPR moves back along the same path towards the X-point. This overlap in both directions indicates that the XPR is continuously in an equilibrium position during this movement. The height inside the confined plasma is determined by the radiative capabilities (i.e. the electron density and impurity concentration) and the power flux into the XPR region. For unfavourable drift direction, the XPR is positioned at the high field side, close to the separatrix. This indicates that the plasma drifts also influence the equilibrium position of the XPR.

The vertical position of the XPR relative to the X-point can be detected and controlled in real time [3], using the impurity seeding level as the actuator. The implemented control regulates the XPR position within 5 mm and controls it reliably up to 10 cm above the X-point, see Fig. 3.

The same control scheme is also applied to control the MARFE induced by fuelling, further indicating that an XPR and MARFE are the same phenomenon. In this way the control is used for disruption avoidance close to the H-mode density limit [14].

4.1.2. ELM suppression

A suppression of ELMs is observed at AUG if the XPR is more than ~7 cm above the X-point [3]. The transition to ELM suppression occurs rather abruptly and is reversible as shown in Fig. 3 (highlighted in green). Several characteristics of the plasma, such as the line averaged density and the stored energy, reduce simultaneously. Throughout the initialization and movement of the XPR, the neutral pressure in the sub-divertor region does not decrease (see Fig. 3f). On the contrary, the neutral compression ($n_{0,div}/n_{0,main}$) might even further increase, which would be essential for efficient pumping in future machines.

In the ELM suppressed phase, the confinement factor H_{98} is in the range of 0.7–1 and the Greenwald density fraction around 0.7–0.8 [7]. The divertor remains fully detached and the intermittent heat and particle bursts by ELMs are absent. It cannot be concluded whether this phase is an L- or an H-mode, as most characteristics, for example the SOL filamentary transport or the pedestal radial electric field, are between the typical values of both confinement regimes [3].

The gradient of the pedestal profiles of electron density and temperature, shown in Fig. 3g & h, are both reduced in the ELM suppressed phase. The pedestal becomes peeling–ballooning stable. Also L-mode like plasmas can feature similar pedestal structures [48]. The reduction in confinement is, at least partially, compensated by an increased temperature gradient from the pedestal top further inside. Although the XPR remains localized at the foot of the pedestal when mapped to the midplane ($\rho_{pol} \geq 0.985$), the pressure gradient reduction extends further inward. The underlying mechanism responsible for the reduced pedestal is not yet identified [3]. For example, increased transport at the foot of the pedestal can reduce the pedestal gradient further-in, as observed in the quasi-continuous exhaust regime [49].

4.2. JET

Soon after the establishment of the XPR as a viable scenario at AUG, the XPR was also identified at JET in highly seeded discharges, first with nitrogen [13] and later with neon, argon and krypton seeding [4]. The ratio of confined volume to separatrix area (or major radius) is higher at JET than at AUG. Therefore, the radiation losses inside the confined region play a bigger role, and scenarios with strong seeding are prone to back-transitions from H- to L-mode or dithering between L- and H-mode [4]. In the H-mode phases with an XPR present the divertor is detached, while in the successive L-modes, the divertor radiation is mainly located in the SOL and the plasma is attached. In the early observations at JET, the operational range with an XPR was limited due to a low heating power and the resulting L-H dithering. Therefore, detailed investigations of the XPR were not possible.

The seeded scenarios could be further stabilized with additional heating power, as it was available in the campaigns of 2022-2023 [50,51]. The XPR investigations in these recent campaigns concentrated on stabilizing the scenario (Section 4.2.1), developing a control scheme for the XPR (Section 4.2.2) and deploying the XPR and its control in deuterium–tritium experiments (Section 4.2.3). The dedicated investigations of the XPR used a low triangularity shape with vertical inner

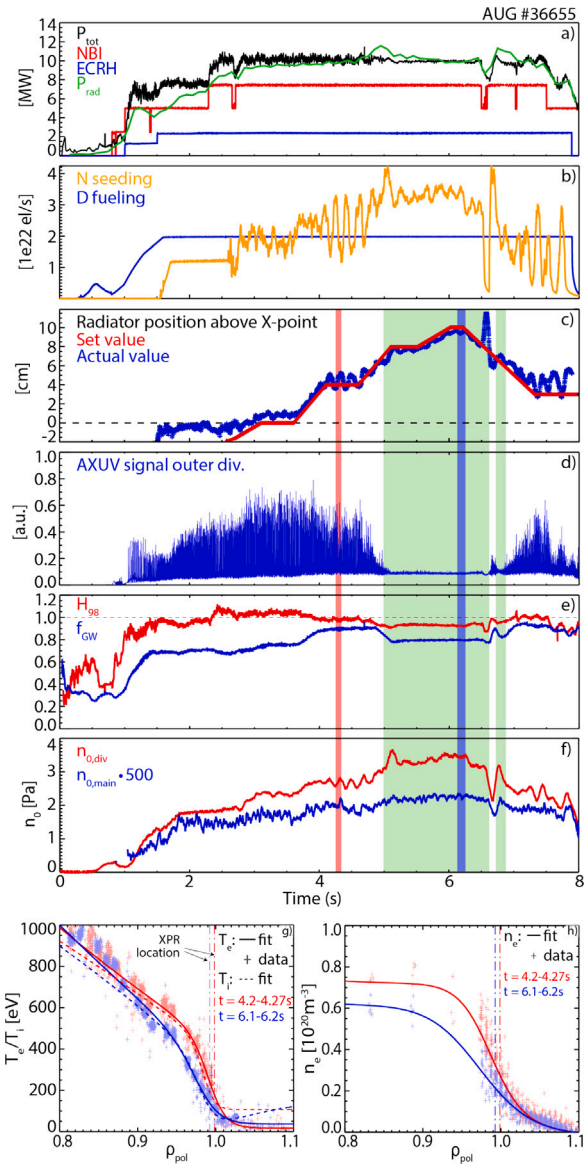

Fig. 3. AUG #36655 demonstrating the XPR control and showing the ELM suppressed phase (green). (a) Heating and radiated power; (b) Deuterium fuelling and nitrogen seeding level; (c) XPR position relative to the X-point; (d) ELM indicator (divertor radiation); (e) H_{98} confinement factor and Greenwald fraction; (f) Neutral gas pressure in the sub-divertor and main chamber (assuming the ionization gauge sensitivity of deuterium for all gases); (g) & (h) pedestal kinetic profiles with (red) and without (blue) ELMs. (For a coloured version of this figure, the reader is referred to the web version of this article.).
Source: Adapted from [3].

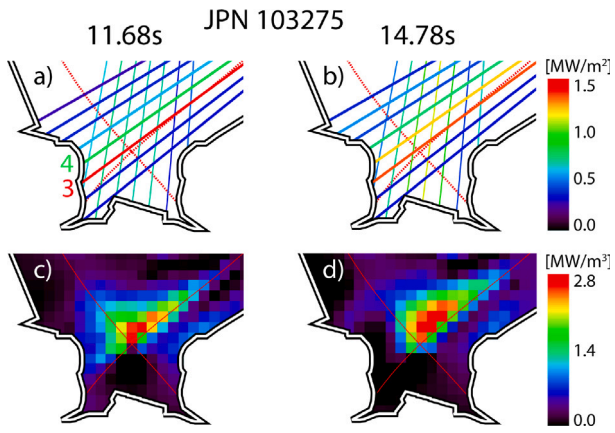

Fig. 4. LOS measurements and tomographic reconstructions from JPN 103275 (H-mode with Ne (FF) and Ar (FB) seeding, similar to Fig. 5). Different XPR heights are achieved by increasing the feedback request value of the XPR height, leading to an emerging XPR (a & c, 11.7 s) and the XPR at the highest observed location (b & d, 14.8 s). (For a coloured version of this figure, the reader is referred to the web version of this article.).

and outer target. Such a scenario is very sturdy against disturbances but has a rather low performance ($H_{98} \approx 0.7$). In high performance plasmas ($H_{98} \approx 0.8 - 0.9$) at high triangularity, the XPR was observed only transiently [52], but not investigated in detail.

4.2.1. Impurities & mixtures

In the recent campaigns the XPR was initiated by nitrogen, neon or argon seeding. With pure neon or argon seeding the plasma still exhibits L-H dithering, even at heating powers of up to 26 MW. This is either caused by too high core radiation losses (Ar) or by the impurity transport in the pedestal (Ne, [4]). The dithering could be prevented by adding nitrogen to the seeding, or by pure N_2 seeding. However, such scenarios would not be applicable for the D–T campaign, where N_2 is not permitted due to the technical constraints of the tritium handling plant. Therefore, also mixtures of Ar and Ne were tested: From pure Ar with a core concentration of up to $c_{Ar} \approx 0.8\%$ (estimated from Z_{eff} measurements), to pure Ne with up to $c_{Ne} = 2\%$ (measured via CXRS). For the latter case, the Ne concentration at the X-point is estimated by spectroscopy [53] to be around 6–10%. With the mixed seeding, the scenarios exhibit an XPR and avoid the L-H dithering. The dithering reappears if either Ne or Ar become too dominant, as then either of the two aforementioned effects start dominating, but can be avoided in a broad range of mix ratios.

The plasmas with an XPR are fully detached and have a radiated power fraction of 65–75% (the maximum stably observed at JET [54]). ELM suppression was also observed at JET. However, the ELMs became continuously smaller and, thus, diminish transiently instead of abruptly like at AUG. For the extreme values of seeding, it cannot be concluded if very small ELMs (relative change of stored energy $\frac{dW_{MHD}}{W_{MHD}} \ll 1\%$) still exist or only broad band fluctuations and filaments are expelled from the confined plasma.

4.2.2. Movement & control

A movement of the XPR can be identified using the horizontal bolometry camera KB5H [55]. The XPR mainly exists within two lines of sight of the KB5H camera (see Fig. 4). The viewing geometry is not optimal, as divertor radiation and XPR radiation overlap in the same LOS. With the help of the vertical camera KB5V, the XPR radiation can be localized inside the confined plasma.

The spatial resolution is significantly reduced relative to the AUG system, and since the LOS of the horizontal camera pass diagonally through the divertor region, a vertical or radial movement cannot be clearly distinguished. Nevertheless, a change of the ratio of the radiation along channels 3 and 4 is interpreted as a vertical shift of the radiation inside the confined region. The real time algorithm described in [14] can determine the peak location of the radiation measured by KB5H with sub-channel resolution, resulting in a continuous measurement through the channels. The channel number is used as the tracking coordinate (see Fig. 5f), as opposed to the mapping onto the vertical distance to the X-point in real space, as done at AUG. As soon as the XPR is present, the real time detected peak location is above 3.2 [measured in KB5H channel number]. Therefore, this value is interpreted as lowest possible location of the XPR. Lower values are a spurious detection of radiation in the divertor SOL volume. At an XPR location of 3.4 the ELMs become insignificantly small and at 3.45 the ELMs fully vanish in the tested regime. The XPR exists up to 3.65 before the plasma disrupts, the highest controllable location is about 3.6.

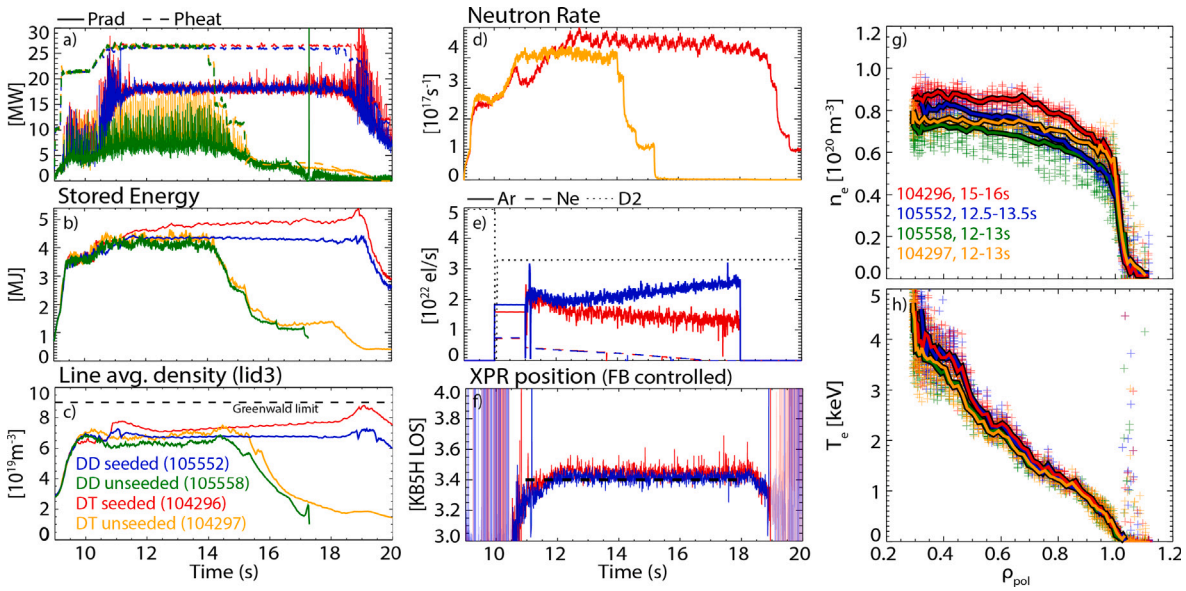

Fig. 5. Seeded (blue & red) and unseeded reference (green & orange) discharges for JET XPR studies in D (blue & green) and DT (red & orange) plasmas. (a) Heating and radiated power; (b) Stored energy W_{dia}; (c) Line averaged density and Greenwald limit; (d) Neutron production rate; (e) Gas fuelling traces (Ar in feedback 11–18 s, Ne & D2 in feed forward); (f) Real-time detection of XPR position; (g) Electron density and (h) electron temperature profiles averaged over the given time windows, measured by Thomson scattering. (For a coloured version of this figure, the reader is referred to the web version of this article.).

The active control is implemented using Ar seeding as the actuator. In order to maintain a mixture of both impurities, Ne is programmed in feed forward, anticipating the required seeding level. As the operational range of the seeding mixture is rather broad, only a rough estimate is needed, the control ensures the correct absolute amount of impurity injection. The gains of the PI control were optimized applying the system identification method [56]. In this way the controller also allows experiments where Ne is continuously reduced and automatically replaced by Ar, scanning a broad range of impurity mixtures while maintaining the same power exhaust capability. An example of such experiments in D plasmas and DT plasmas in shown in Fig. 5.

The control loop reacts much more slowly at JET (time scale of ~ 1 s) than at AUG (~ 200 ms). This is dominantly due to slower reacting valves and long pipes in-between the valve and the opening to the torus. Despite the long delays, the control works remarkably well and the XPR can be controlled within 1/20th of the channel spacing of KB5H, i.e. within about 4 mm in height above the X-point.

4.2.3. D–D and D–T plasmas

Fig. 5 shows a comparison of D and DT plasmas with an XPR with their unseeded counterparts. The unseeded discharges are shorter in duration to prevent overheating of the divertor, which is not a concern for the seeded discharges.

For both seeded discharges, the XPR control was active and the feed forward programmed Ne injection is continuously ramped down. This leads to a changeover from a mixed Ar+Ne seeding to pure Ar seeding, while the XPR is kept at a height of 3.4. In the case of the DT plasma, the Ar seeding decreases (red trace in Fig. 5e), as is expected due to the increasing impurity wall storage which eventually saturates. Such a behaviour is observed in most seeding experiments, also at AUG. The reason for the atypical increase of Ar seeding for the D plasma (blue trace in Fig. 5e) is not known, but it might be influenced by a reduced wall loading in the preceding discharges.

The radiated power fraction increases with the creation of the XPR from about 25% up to 70%, reflecting the highest values in JET for pulses with significant heating power [54]. The stored energy, and with this the energy confinement time, of the seeded plasmas is slightly higher than the unseeded ones. The kinetic profiles in Fig. 5 g & h indicate that this improved confinement is due to an increased density and slightly increased electron temperature in the region $\rho_{pol} \leq 0.9$. This can be at least partially explained by the stabilization of ITG turbulence in the core of the plasma due to the dilution by impurities [5], an effect which is not necessarily scalable to a reactor [48]. A more crucial finding is that the edge (i.e. the pedestal top pressure) is not deteriorated by the presence of the XPR in the plasma, even if the ELMs are suppressed. This is in contrast to the observations at AUG.

The main noticeable change between the D and the DT plasmas is the increased density from the pedestal top inwards for the DT plasmas, which is within the expectations and observed for most DT experiments at JET [57–59]. In the DT plasmas, up to 1.25 MW of fusion power was produced. Since only 0.25 MW was carried by alpha particles, the additional heating power is negligible.

The experiments at JET show that the presence of the XPR is independent of the main ion isotope and that the XPR is compatible with the fuel used in future reactors. With an increased device size, the XPR becomes more resilient to perturbations, such as power variations of up to a factor of 2 or the injection of fuelling pellets. However, the energy confinement of the tested scenarios was rather low even before the XPR is formed, in the range of $H_{98} = 0.65 - 0.75$. The experiments show, however, that the presence of an XPR does not lead to a decrease of the pedestal performance in such scenarios.

4.3. XPRs in further devices

Regimes with XPRs have also been observed at other tokamaks. At TCV, the XPR was first observed in nitrogen seeded L-modes [6], then in seeded H-modes [7] and unseeded snowflake divertor configurations in H-mode [8]. TCV is the first machine with carbon walls to report the existence of an XPR (except the observations shown in Section 2, which were not classified as XPR). The stability window of the operation with an XPR is at TCV smaller than in AUG or JET, most likely due to the presence of intrinsic carbon, the smaller device size or limited available heating power. With an increased flux expansion at the X-point, achieved by a snowflake configuration, the XPR can also be triggered without additional seeding [8], presumably relying on the intrinsic carbon impurity. This highlights again the importance of the flux expansion for the XPR access. In this regime also ELM suppression in H-mode can be observed, similar to the behaviour at AUG. Using the

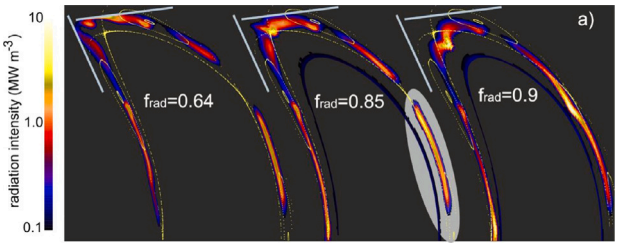

Fig. 6. Radiation distribution in EMC3-Eirene modelling of the stellarator W-7X. At high radiated power fractions the radiation peaks at the X-points of the island divertor and then moves further inwards. (For a coloured version of this figure, the reader is referred to the web version of this article.).
Source: Figure adapted from [62].

filtered camera system MANTIS [60], a real-time control of the XPR location was implemented [7]. However, the operational range is still limited, reflecting the lower stability of the XPR regime in a standard divertor geometry at TCV.

At the WEST tokamak an XPR was achieved with nitrogen seeding in L-mode [10–12]. The transition to the XPR regime occurs on a very fast timescale, indicating a bifurcative behaviour from an attached plasma to a high recycling regime (still attached) with the radiation inside the X-point. The regime with XPR is very stable. An active control, which uses interferometry to detect the high density of the XPR, allows the XPR regime to be maintained for more than 10 s. Due to a lack of H-mode operation at WEST, the XPR existence in H-mode and ELM suppression could not yet be tested. In the XPR scenario, the tungsten contamination of the confined plasma is reduced significantly compared to the standard operation and the phase before the bifurcation, presumably due to the reduced electron temperature at the target, which reduces the tungsten sputtering.

At KSTAR also a bifurcation-like transition from an attached regime to an XPR is observed [9]. This occurs in L-mode density ramp discharges without additional seeding, the intrinsic carbon is expected to trigger the XPR, similar to the TCV snowflake experiments. The experiments could also be reproduced by SOLPS-ITER simulations [9].

At COMPASS a fast transition to an XPR like regime was observed [61] for nitrogen seeded L-modes and could be maintained for about 100 ms.

The XPR phenomenon may also occur in stellarators. For the stellarator Wendelstein-7X (W-7X), EMC3-EIRENE modelling [62,63] shows that at a high radiated power fraction the radiation peaks at the five X-points of the island divertor (see Fig. 6). These peaks move further inwards with a higher radiated fraction, similar to the observations on tokamaks. In experiments, the radiation peak is also observed at the X-points [64], but might as well shift to the O-points of the islands [65], and is not yet observed to move slowly inwards.

The observation at W7-X shows that XPRs are not restricted to toroidally symmetric devices. The ongoing research and the difference in behaviour between stellarators and tokamaks might further shed light on the physics governing the XPR phenomenon.

5. Prediction and application in future devices

The XPR combines several advantages for future reactors: Its high power exhaust capabilities, the simple observable to control the power exhaust, and the potential ELM suppression make it a attractive scenario for future reactors. The possibility of achieving an XPR in ITER or a EU-DEMO-like device [66] is being investigated with SOLPS modelling (Section 5.1). To predict the performance in a future reactor, the required impurity concentration needs to be known (Section 5.2), and the impact on the confinement be understood (Section 5.3). The application of the XPR can be already today envisaged to ease the operation or even construction of a future reactor, as illustrated by two examples in Section 5.4 & 5.5.

5.1. ITER and DEMO SOLPS modelling

The first SOLPS-ITER modelling of an XPR in ITER is discussed in [45]. The simulations use neon as seed impurity and apply all available drift and current contributions. The observations are qualitatively the same as in AUG: a fully detached divertor, a cold X-point of a few eV at high density ($\geq 2 \cdot 10^{20}\,\mathrm{m}^{-3}$) and parallel electron temperature gradients inside the confined region. However, the radiating region of the XPR is shifted towards the outer midplane, dominantly due to the peak of Ne emission around 60 eV. The impurity concentration needed to achieve the XPR in ITER is around 4% at the inner core boundary of the modelling. These values would be too high for a reactor, but the modelling does not reflect the full impurity transport description in the pedestal, and a reduced core penetration of the impurities can be expected for ITER-size devices [67].

For DEMO, as yet only simplified modelling is available [68], scaling the AUG geometry to an EU-DEMO-size device. These simulations were executed without drifts and in the CRD configuration (see Section 5.5). The code results indicate that an XPR could be integrated into large-scale devices, enabling detached scenarios at high exhaust power levels. The impurity concentration at the core boundary are in the range of 0.4% for argon or 0.8% for nitrogen seeding, whereas a trade off between impurity concentration and upstream density can be made ($2.7 \cdot 10^{19}\,\mathrm{m}^{-3}$ for the Ar case vs $3.8 \cdot 10^{19}\,\mathrm{m}^{-3}$ for the N2 case). The simulations exhibit a neutral pressure of more than 10 Pa in the private flux region despite an open divertor geometry and no baffling. In the ITER simulations, the pressure is also remaining high, though reducing with an XPR from about 10 Pa to 6 Pa [45]. This shows also by modelling that in the XPR regime a high neutral compression can be achieved, allowing for efficient neutral pumping for a reactor in such a scenario.

The SOLPS simulations for both devices cannot predict the influence of the XPR and the impurities on the pedestal and core plasma. Therefore, the impact on the overall scenario performance cannot be estimated with these tools, rather integrated modelling is necessary. The SOLPS modelling shows, nonetheless, that an XPR can be accessed in large scale devices.

5.2. Impurity requirements for a reactor

The impurity concentration is an essential ingredient for the prediction of the operational point of a reactor. One has to distinguish between the impurity concentration at the X-point and in the core of the plasma. While the first is the requirement to initiate the XPR, the latter influences the reactor operation by dilution and core radiative losses (for light impurities mainly Bremsstrahlung). Impurities are usually enriched in the divertor volume [69], but this enrichment is not specified for the X-point region.

For AUG, the nitrogen concentration in the core is around 2–3%, while the spectroscopically estimated concentration at the X-point is in the range of 10–20% [53]. For JET with pure Ne seeding, the concentrations are 1.75% in the core and 6–10% at the X-point. The measurements at both tokamaks show a significant enrichment of the impurities at the X-point region. This enrichment is caused, in part, by the neoclassical transport in the pedestal, creating radial concentration gradients [67], but a parallel compression from the upstream location towards the X-point may also contribute. The DEMO SOLPS simulations (Section 5.1) show such parallel compression of impurities towards the X-point.

In the SOLPS simulations for DEMO [44], the impurity concentration at the X-point needed to create an XPR is either 2% nitrogen or 3% argon (with a trade off between upstream density and impurity concentration). The reduction from the current devices to DEMO are in line with expectations, due to the increased major radius and, thus, bigger radiating volume of the XPR region, which scales more strongly

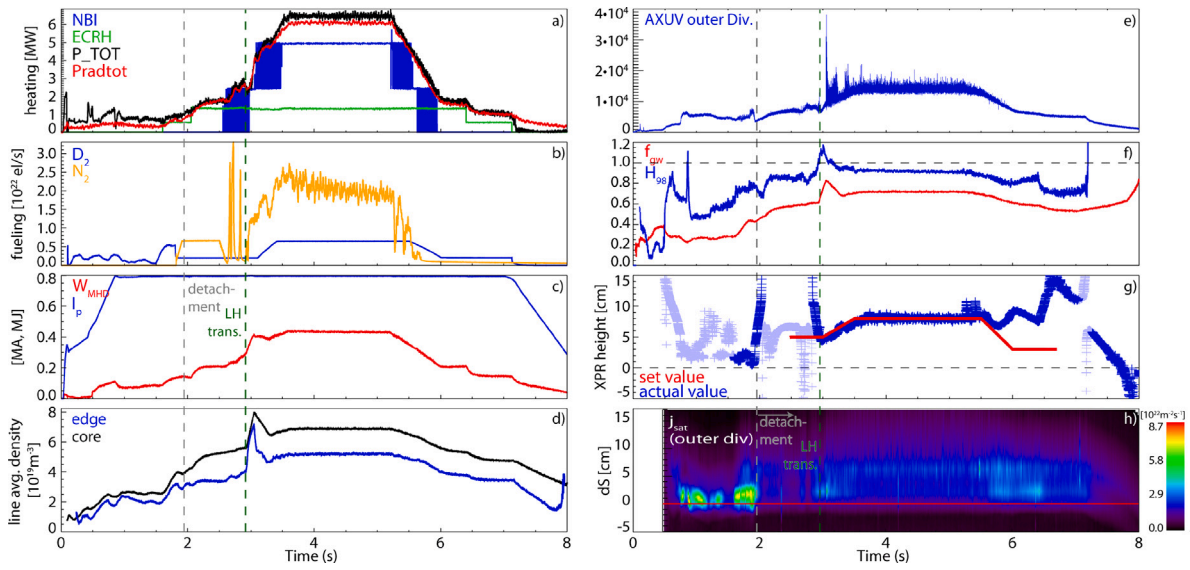

Fig. 7. AUG #40333 demonstrating a fully detached discharge from ramp-up to ramp-down. (a) heating and radiated power; (b) fuelling and seeding; (c) plasma current and stored energy; (d) line averaged density; (e) radiation in the outer divertor; (f) Greenwald fraction and normalized energy confinement; (g) XPR real-time position (spurious detection shown in lighter colour) and set location; (h) ion saturation current to the outer divertor. (For a coloured version of this figure, the reader is referred to the web version of this article.).

than the exhaust power. The expected higher upstream pressure at the separatrix further benefits an XPR.

The DEMO SOLPS modelling results in a concentration at the inner core boundary of 0.8% (N) or 0.4% (Ar) (see Section 5.1). These levels are well within operational boundaries of a reactor (e.g. 2% N or 0.6% Ar at a $\frac{\tau_{He}}{\tau_E} = 5$ [70]). However, the ITER SOLPS modelling shows Ne concentrations at the core boundary of about 4%, which would be too high to achieve burn conditions in a reactor. The difference between the two might depend on the trade off between upstream density and impurity concentration and the influence of drifts (which are not included in the DEMO case) and needs to be further elaborated. Note however, that both cases of modelling do not reflect the full impurity transport. A further reduction of the impurity concentration towards the core is expected from the neoclassical impurity transport in the pedestal of such large scale devices [67]. In order to reliably predict the core contamination with impurities for a reactor, integrated modelling taking into account the SOL, pedestal and core physics is necessary, but not yet available.

5.3. Impact on confinement

In order to predict the full impact of an XPR on a future reactor scenario, the influence on the energy confinement has to be understood. Such a prediction is not yet possible, since the interaction of impurities with the pedestal is unclear. The peeling–ballooning theory is not directly applicable, as resistive effects start to play a bigger role. With the existence of an XPR inside the plasma, further effects, such as the local cooling and the poloidal asymmetries might also impact the pedestal.

In current devices, the XPR either leads to a small reduction of the energy confinement time (AUG), or to a small increase (JET). For JET, the increase is related to a suppression of core ITG modes [5], while the pedestal remains unchanged within the measurement uncertainty when the XPR enters the plasma (see Fig. 5). However, for the JET experiments the unseeded reference plasma had a low energy confinement ($H_{98} \approx 0.65$), which increased with seeding to about $H_{98} \approx 0.7 - 0.8$. For AUG, the confinement factor is in the range of $H_{98} = 0.8 - 1.1$ with ELMs or $H_{98} = 0.7 - 1$ in ELM suppression. The access to ELM suppression comes at a cost of reduced energy confinement.

This contrary behaviour of the different devices must be further understood before the energy confinement of a reactor can be predicted. For this, detailed pedestal analysis is required and the influence of the impurities on the pedestal needs to be understood. The experiments show, nonetheless, that a good confinement might be possible, but a reduction of the confinement relative to the unseeded case is to be expected.

5.4. Detached ramp-up & -down

For future reactors, not only the flattop of the discharge needs to be detached, but also the transients, such as the ramp-up and -down of the discharge. This is needed to maintain a reliable divertor operation. The ramp-up includes the L-H transition, during which the power flow to the divertor changes massively, due to the increase of external heating power ($P_{div} \uparrow$), the increase of stored energy ($P_{div} \downarrow$) and the shrinking of the heat flux channel from L- to H-mode ($\lambda_q \downarrow$). These transients need to be compensated while avoiding reattachment or a radiative collapse.

The XPR, with its wide operational range of vertical movement, offers a buffer which withstands such changes. This was demonstrated at AUG, see Fig. 7. After a reference phase in L-mode (up to 1.8 s), nitrogen is first injected in feed forward to trigger an XPR (1.8–2.4 s). The seeding values were iterated in feed forward based on preceding discharges, as the XPR control is not yet tuned for L-mode discharges at low power. With the beginning of the seeding, the divertor immediately detaches and the XPR moves upwards, outside the viewing volume for the real time detection. The XPR control is then activated and the NBI power smoothly ramped up by pulse width modulation. The L–H transition occurs during this ramp at 2.9 s, indicated by an strong increase of electron density, plasma stored energy and changed divertor radiation. A few ELMs appear after the transition, but are almost completely buffered before reaching the divertor and only show a slight increase of ion saturation current away from the strikeline. At the XPR request location of 8 cm ELMs are suppressed and only broad band, high frequency fluctuations or filaments can be observed. After the

flattop phase the power is ramped down in parallel with the XPR request location. The seeding is automatically turned off, as the XPR is higher than the request location and the pump out of the nitrogen occurs on a slower time scale. Due to the slow reduction of the power, the XPR does not move too high and the plasma remains stable and detached. During this phase the H–L transition occurs, but the exact timing cannot be identified as the typical indicators for a L–H transition change transiently instead of abruptly. Such a behaviour is often seen at high density H–L transitions [71]. The detachment is maintained throughout this transition. Also during the current and shape ramp down the XPR is still present in the plasma, and a disruption only occurs at a third of the original plasma current when the plasma is moving out of the divertor configuration.

This shows that an XPR makes it possible to maintain detachment throughout the L–H transition and demonstrates the first detached ramp up of a tokamak discharge. A more rapid detached ramp up was afterwards also used in combination with other physics investigations, showing a good reproducibility of such scenarios.

For the ramp up in a reactor, the high amount of injected impurities (here around 3% with up to 3.5% during the transition) would lead to a higher consumption of the flux swing of the central solenoid and, thus, reduce the possible pulse duration. Also the interplay between the time scales of power fluxes and gas fluxes and pumping times have to be studied in more detail and require elaborate modelling before such a scenario can be planned for a reactor. The experiments prove, however, that detached L–H transitions and ramp ups are physically possible by utilizing an XPR.

5.5. Compact radiative divertor

If a future reactor would operate with an XPR, the requirements for the divertor might be significantly alleviated. It might be possible to reduce the divertor size and simplify its structures. This idea is embodied in the so-called compact radiative divertor (CRD) [72]: the combination of an XPR scenario with the minimal necessary divertor volume. In this case the X-point is placed close to or on the divertor target tiles. Contrary to a limiter plasma, an X-point geometry is still necessary in order to create a region with high flux expansion.

The exhaust power is dissipated by the XPR before it reaches the target. Therefore, the shallow inclination angles of the field lines on the target ($< 0.5°$) are not critical. For conventional configurations these have to be larger than 2–3° [73,74] to avoid overheating at leading edges of tile gaps. By minimizing the divertor volume, the reactor can accommodate a larger confined plasma, leading to increased power production or enabling a more compact reactor design. This comes, however, with the caveat of the high impurity concentration to maintain the XPR. Additionally, the divertor structures become simpler, as the deposited power is significantly reduced and dominated by radiation instead of charged particles. As the shaping is relaxed, the currents through the poloidal field coils are lower, reducing their complexity and increasing the vertical stability of the plasma [72].

In order to test the CRD, experiments at AUG were executed, where first an XPR was created, then the X-point moved towards the divertor plates. These experiments prove that the resulting heat loads are manageable and even tile displacements of several millimeters do not cause overheating or damage. The active XPR control and its wide operational range helped to compensate heat perturbations, which were applied to provoke reattachment, but were successfully buffered.

In the experiments at AUG, the neutral compression in the divertor ($\frac{n_{0,div}}{n_{0,main}}$) was maintained despite the full detachment and open divertor geometry. SOLPS modelling [68] also showed that the neutral pressure in the divertor region of a reactor scale device can be higher than 10 Pa. Therefore, not only power, but also particle exhaust can be ensured in such configurations.

Further studies are needed to quantify the benefits of a CRD configuration in the integrated design of a DEMO power plant, to further assess the particle exhaust, specifically for helium, and to estimate the impurity concentration and performance such a configuration could provide. Specifically the reattachment has to be avoided by all means in such a device (though a conventional divertor has similar requirements). The initial experiments with a CRD showed that it is possible to operate in such configurations and the SOLPS studies showed that it is also accessible in a reactor scale device. This can significantly alleviate the requirements for a future reactor and ease its realization.

6. Conclusion

In 2012, X-point radiation was recognized at AUG as a stable regime which might have several beneficial properties in a metal wall machine, and was extensively studied since then. It is an attractive reactor scenario, as it offers highest radiated power fractions and full detachment with a clear observable and a wide operational range. Additionally, the presence of an XPR may provide access to an ELM-suppressed regime, and, thus, fulfill one more requirement for a reactor scenario. This does, however, come at the cost of an increased impurity concentration and a potential reduction in confinement.

While in the 1980s to 2000s, similar effects were occasionally observed, such a regime was not investigated further, as the observation of radiation at the X-point was associated with disruptions and a reduced confinement, making it not attractive for a reactor. Now, however, stable XPRs are observed on almost all operating tokamaks. The successful demonstration of the XPR existence and control in JET's DT experiments substantiate its potential application in future devices.

Analytical models and SOLPS-ITER simulations of the XPR further deepen the understanding of the phenomenon and allow first tentative extrapolations to future reactors. Emerging simulations with other large scale codes, such as Grillix, JOREK and SOLEDGE3X, help to investigate different aspects of the XPR regime, such as MHD stability and turbulence characteristics.

In order to predict the behaviour in a future reactor, more work on the XPR regime is required. Since the access to an XPR requires a high impurity content at the X-point, the transport of these impurities into the core of the plasma has to be understood, and potentially be reduced. Furthermore, the impact on the confinement needs to be minimized. For this the understanding of the edge plasma in the presence of such strong poloidal asymmetries and high impurity concentrations needs to be improved. The process which leads to the reduction of pedestal gradients and, thus, to the ELM suppression, needs further investigation to clarify the mechanisms at play. A reliable prediction of the XPR behaviour and its impact in a future reactor requires integrated modelling, which takes into account the full impurity transport and the coupling between the SOL, edge and core plasma.

Even without such integrated modelling, several benefits of an XPR for a reactor scale device can already be anticipated: the many desirable features such as detachment, controllability, and ELM suppression, together with the potential to simplify the divertor, make it an attractive option for the operation in a future reactor.

CRediT authorship contribution statement

M. Bernert: Writing – original draft, Visualization, Project administration, Investigation, Conceptualization. **T.O.S.J. Bosman:** Investigation, Conceptualization. **T. Lunt:** Investigation, Conceptualization. **O. Pan:** Investigation. **B. Sieglin:** Software, Methodology, Investigation, Conceptualization. **U. Stroth:** Writing – review & editing, Investigation, Conceptualization. **A. Kallenbach:** Writing – review & editing, Investigation. **S. Wiesen:** Investigation. **M. Wischmeier:** Writing – review & editing, Supervision, Investigation, Conceptualization. **G. Birkenmeier:** Investigation. **M. Cavedon:** Investigation. **B. Lipschultz:** Investigation, Conceptualization. **C. Lowry:** Investigation, Conceptualization. **N. Fedorczak:** Investigation. **P. Fox:** Software, Investigation.

M. Lennholm: Investigation. **H. Sun:** Investigation. **P. Jacquet:** Investigation. **K. Kirov:** Investigation. **N. Vianello:** Supervision, Investigation. **D. Brida:** Investigation. **S. Henderson:** Investigation, Conceptualization. **P. David:** Software, Investigation. **R. Dux:** Investigation. **R.M. McDermott:** Writing – review & editing, Investigation. **H. Reimerdes:** Supervision, Investigation, Conceptualization. **C. Theiler:** Investigation. **M. Komm:** Investigation. **O. Février:** Investigation. **U. Sheikh:** Investigation. **S. Menmuir:** Validation, Investigation. **J.T.W. Koenders:** Software, Investigation. **L. Ceelen:** Software, Investigation. **M.G. Dunne:** Investigation. **O. Kudlacek:** Software, Investigation. **F. Reimold:** Investigation.

Declaration of competing interest

The authors declare the following financial interests/personal relationships which may be considered as potential competing interests: Matthias Bernert reports financial support was provided by European Consortium for the Development of Fusion Energy. If there are other authors, they declare that they have no known competing financial interests or personal relationships that could have appeared to influence the work reported in this paper.

Acknowledgements

This work has been carried out within the framework of the EUROfusion Consortium, partially funded by the European Union via the Euratom Research and Training Programme (Grant Agreement No 101052200 - EUROfusion). The Swiss contribution to this work has been funded by the Swiss State Secretariat for Education, Research and Innovation (SERI). Views and opinions expressed are however those of the author(s) only and do not necessarily reflect those of the European Union, the European Commission or SERI. Neither the European Union nor the European Commission nor SERI can be held responsible for them.

Data availability

Data will be made available on request.

References

[1] F. Reimold, M. Wischmeier, M. Bernert, et al., Experimental studies and modeling of complete H-mode divertor detachment in ASDEX Upgrade, J. Nucl. Mater. 463 (2015) 128–134, http://dx.doi.org/10.1016/j.jnucmat.2014.12.019, PLASMA-SURFACE INTERACTIONS 21.

[2] F. Reimold, M. Wischmeier, M. Bernert, et al., Divertor studies in nitrogen induced completely detached H-modes in full tungsten ASDEX Upgrade, Nucl. Fusion 55 (3) (2015) 033004, http://dx.doi.org/10.1088/0029-5515/55/3/033004.

[3] M. Bernert, F. Janky, B. Sieglin, et al., X-point radiation, its control and an ELM suppressed radiating regime at the ASDEX Upgrade tokamak, Nucl. Fusion 61 (2) (2020) 024001, http://dx.doi.org/10.1088/1741-4326/abc936.

[4] M. Bernert, M. Wischmeier, A. Huber, et al., Power exhaust by SOL and pedestal radiation at ASDEX Upgrade and JET, Nucl. Mater. Energy 12 (2017) 111–118, http://dx.doi.org/10.1016/j.nme.2016.12.029, Proceedings of the 22nd International Conference on Plasma Surface Interactions 2016, 22nd PSI.

[5] S. Glöggler, M. Wischmeier, E. Fable, et al., Characterisation of highly radiating neon seeded plasmas in JET-ILW, Nucl. Fusion 59 (12) (2019) 126031, http://dx.doi.org/10.1088/1741-4326/ab3f7a.

[6] O. Février, C. Theiler, J.R. Harrison, et al., Nitrogen-seeded divertor detachment in TCV L-mode plasmas, Plasma Phys. Control. Fusion 62 (3) (2020) 035017, http://dx.doi.org/10.1088/1361-6587/ab6b00.

[7] M. Bernert, S. Wiesen, O. Février, et al., The X-Point radiating regime at ASDEX Upgrade and TCV, Nucl. Mater. Energy 34 (2023) 101376, http://dx.doi.org/10.1016/j.nme.2023.101376.

[8] H. Reimerdes, C. Theiler, M. Bernert, et al., Access to an ELM-suppressed X-point radiator regime in TCV snowflake minus configurations, Nucl. Mater. Energy 41 (2024) 101784, http://dx.doi.org/10.1016/j.nme.2024.101784.

[9] J.-S. Park, R. Pitts, J. Jang, et al., Bifurcation-like transition of divertor conditions induced by X-point radiation in KSTAR L-mode plasmas, Nucl. Fusion 63 (8) (2023) 086018, http://dx.doi.org/10.1088/1741-4326/acdefe.

[10] J. Bucalossi, A. Ekedahl, the WEST Team, et al., WEST full tungsten operation with an ITER grade divertor, Nucl. Fusion 64 (11) (2024) 112022, http://dx.doi.org/10.1088/1741-4326/ad64e5.

[11] N. Rivals, N. Fedorczak, P. Tamain, et al., Experiments and SOLEDGE3X modeling of dissipative divertor and X-point Radiator regimes in WEST, Nucl. Mater. Energy 40 (2024) 101723, http://dx.doi.org/10.1016/j.nme.2024.101723.

[12] N. Fedorczak, et al., The X-point radiator regime in WEST, 2025, (in preparation).

[13] M. Wischmeier, High density operation for reactor-relevant power exhaust, J. Nucl. Mater. 463 (2015) 22–29, http://dx.doi.org/10.1016/j.jnucmat.2014.12.078, PLASMA-SURFACE INTERACTIONS 21.

[14] B. Sieglin, M. Maraschek, A. Gude, et al., Disruption avoidance and investigation of the H-Mode density limit in ASDEX Upgrade, Plasma Phys. Control. Fusion 66 (2) (2023) 025004, http://dx.doi.org/10.1088/1361-6587/ad163a.

[15] B. Lipschultz, B. LaBombard, E. Marmar, et al., Marfe: an edge plasma phenomenon, Nucl. Fusion 24 (8) (1984) 977, http://dx.doi.org/10.1088/0029-5515/24/8/002.

[16] U. Samm, G. Bertschinger, P. Bogen, et al., Plasma edge cooling by impurity radiation in a tokamak, Plasma Phys. Control. Nucl. Fusion Res. (1993) A–5–3.

[17] U. Stroth, M. Bernert, D. Brida, et al., Model for access and stability of the X-point radiator and the threshold for marfes in tokamak plasmas, Nucl. Fusion 62 (7) (2022) 076008, http://dx.doi.org/10.1088/1741-4326/ac613a.

[18] J. Wesson, R. Gill, M. Hugon, et al., Disruptions in JET, Nucl. Fusion 29 (4) (1989) 641, http://dx.doi.org/10.1088/0029-5515/29/4/009.

[19] M. Maraschek, A. Gude, V. Igochine, et al., Path-oriented early reaction to approaching disruptions in ASDEX Upgrade and TCV in view of the future needs for ITER and DEMO, Plasma Phys. Control. Fusion 60 (1) (2017) 014047, http://dx.doi.org/10.1088/1361-6587/aa8d05.

[20] U. Samm, M. Brix, F. Durodié, et al., MARFE feedback experiments on TEXTOR-94, J. Nucl. Mater. 266–269 (1999) 666–672, http://dx.doi.org/10.1016/S0022-3115(98)00516-9.

[21] V. Mertens, M. Kaufmann, J. Neuhauser, et al., High density operation close to Greenwald limit and H mode limit in ASDEX Upgrade, Nucl. Fusion 37 (11) (1997) 1607, http://dx.doi.org/10.1088/0029-5515/37/11/I10.

[22] C. Lowry, D. Campbell, S. Davies, et al., Divertor configuration studies on JET, J. Nucl. Mater. 241–243 (1997) 438–443, http://dx.doi.org/10.1016/S0022-3115(97)80078-5.

[23] G. Matthews, B. Balet, J. Cordey, et al., Studies in JET divertors of varied geometry. II: Impurity seeded plasmas, Nucl. Fusion 39 (1) (1999) 19, http://dx.doi.org/10.1088/0029-5515/39/1/302.

[24] O. Gruber, A. Kallenbach, M. Kaufmann, et al., Observation of continuous divertor detachment in H-Mode discharges in ASDEX Upgrade, Phys. Rev. Lett. 74 (1995) 4217–4220, http://dx.doi.org/10.1103/PhysRevLett.74.4217.

[25] J. Neuhauser, M. Alexander, G. Becker, et al., The compatibility of high confinement times and complete divertor detachment in ASDEX-Upgrade, Plasma Phys. Control. Fusion 37 (11A) (1995) A37, http://dx.doi.org/10.1088/0741-3335/37/11A/003.

[26] A. Kallenbach, R. Dux, V. Mertens, et al., H mode discharges with feedback controlled radiative boundary in the ASDEX Upgrade tokamak, Nucl. Fusion 35 (10) (1995) 1231, http://dx.doi.org/10.1088/0029-5515/35/10/I07.

[27] A. Kallenbach, R. Dux, H.-S. Bosch, et al., Radiative boundary discharges with impurity injection and the H-L transition in ASDEX Upgrade, Plasma Phys. Control. Fusion 38 (12) (1996) 2097, http://dx.doi.org/10.1088/0741-3335/38/12/005.

[28] P.E. Vandenplas, A.M. Messiaen, J.P.H.E. Ongena, et al., Review and present status of the TEXTOR radiative improved (RI) mode, J. Plasma Phys. 59 (4) (1998) 587–610, http://dx.doi.org/10.1017/S0022377898006734.

[29] J.A. Goetz, C. Kurz, B. LaBombard, et al., Comparison of detached and radiative divertor operation in Alcator C-Mod, Phys. Plasmas 3 (5) (1996) 1908–1915, http://dx.doi.org/10.1063/1.871986.

[30] R. Pitts, A. Refke, B. Duval, et al., Experimental investigation of the effects of neon injection in TCV, J. Nucl. Mater. 266–269 (1999) 648–653, http://dx.doi.org/10.1016/S0022-3115(98)00599-6.

[31] N. Asakura, H. Hosogane, S. Tsuji-Iio, et al., Field reversal effects on divertor plasmas under radiative and detached conditions in JT-60U, Nucl. Fusion 36 (6) (1996) 795, http://dx.doi.org/10.1088/0029-5515/36/6/I10.

[32] ITER Physics Basis Editors and ITER Physics Expert Group Chairs and Co-Chairs and ITER Joint Central Team and Physics Integration Unit, Chapter 1: Overview and summary, Nucl. Fusion 39 (12) (1999) 2137, http://dx.doi.org/10.1088/0029-5515/39/12/301.

[33] A. Loarte, B. Lipschultz, A. Kukushkin, et al., Chapter 4: Power and particle control, Nucl. Fusion 47 (6) (2007) S203, http://dx.doi.org/10.1088/0029-5515/47/6/S04.

[34] J. Paméla, JET under EFDA: organisation, recent results and prospects, Fusion Eng. Des. 56–57 (2001) 19–28, http://dx.doi.org/10.1016/S0920-3796(01)00232-0.

[35] O. Pan, M. Bernert, T. Lunt, et al., SOLPS-ITER simulations of an X-point radiator in the ASDEX Upgrade tokamak, Nucl. Fusion 63 (1) (2022) 016001, http://dx.doi.org/10.1088/1741-4326/ac9742.

[36] M. Siccinio, W. Biel, M. Cavedon, et al., DEMO physics challenges beyond ITER, Fusion Eng. Des. 156 (2020) 111603, http://dx.doi.org/10.1016/j.fusengdes.2020.111603.
[37] T. Eich, B. Sieglin, A. Scarabosio, et al., Inter-ELM power decay length for JET and ASDEX Upgrade: Measurement and comparison with heuristic drift-based model, Phys. Rev. Lett. 107 (2011) 215001, http://dx.doi.org/10.1103/PhysRevLett.107.215001.
[38] A. Kallenbach, M. Bernert, R. Dux, et al., Impurity seeding for tokamak power exhaust: from present devices via ITER to DEMO, Plasma Phys. Control. Fusion 55 (12) (2013) 124041, http://dx.doi.org/10.1088/0741-3335/55/12/124041.
[39] M. Bernert, Analysis of the H-mode Density Limit in the ASDEX Upgrade Tokamak Using Bolometry (Ph.D. thesis), Ludwig-Maximilians-Universität München, 2013, http://dx.doi.org/10.5282/edoc.16262.
[40] S. Wiesen, D. Reiter, V. Kotov, et al., The new SOLPS-ITER code package, J. Nucl. Mater. 463 (2015) 480–484, http://dx.doi.org/10.1016/j.jnucmat.2014.10.012, PLASMA-SURFACE INTERACTIONS 21.
[41] I. Senichenkov, E. Kaveeva, V. Rozhansky, et al., Detached regime with highly radiating X-point physics and modelling, Contrib. Plasma Phys. 62 (5–6) (2022) e202100177, http://dx.doi.org/10.1002/ctpp.202100177.
[42] G. Sun, SOLPS-ITER simulation of an X-point radiator in TCV, 2023, (submitted for publication).
[43] K. Eder, W. Zholobenko, A. Stegmeir, et al., Fluid modeling of plasma-neutrals turbulence in detached regimes, in: 26th International Conference on Plasma Surface Interaction in Controlled Fusion Devices, PSI, Marseille, FR, 2024.
[44] O. Pan, M. Bernert, T. Lunt, et al., Analysis of the generation and poloidal size of X-point radiators in AUG, JET, and EU-DEMO using SOLPS-ITER modelling, in: 50th EPS Conference of Plasma Physics, Salamanca, ES, 2024.
[45] A. Poletaeva, V. Rozhansky, E. Kaveeva, et al., First SOLPS-ITER modelling of an X-point radiator in ITER, Nucl. Fusion 64 (12) (2024) 126038, http://dx.doi.org/10.1088/1741-4326/ad7ed4.
[46] A. Kallenbach, M. Bernert, M. Beurskens, et al., Partial detachment of high power discharges in ASDEX Upgrade, Nucl. Fusion 55 (5) (2015) 053026, http://dx.doi.org/10.1088/0029-5515/55/5/053026.
[47] M. Bernert, T. Eich, A. Burckhart, et al., Application of AXUV diode detectors at ASDEX Upgrade, Rev. Sci. Instrum. 85 (3) (2014) 033503, http://dx.doi.org/10.1063/1.4867662.
[48] E. Fable, A. Kallenbach, R. McDermott, et al., High-confinement radiative L-modes in ASDEX Upgrade, Nucl. Fusion 62 (2) (2021) 024001, http://dx.doi.org/10.1088/1741-4326/ac3e81.
[49] G.F. Harrer, M. Faitsch, L. Radovanovic, et al., Quasicontinuous exhaust scenario for a fusion reactor: The renaissance of small edge localized modes, Phys. Rev. Lett. 129 (2022) 165001, http://dx.doi.org/10.1103/PhysRevLett.129.165001.
[50] E. Joffrin for the JET contributors and the EUROfusion Tokamak Exploitation Team, 66th Annual Meeting of the APS Division of Plasma Physics, Atlanta, USA, 2024.
[51] A. Kappatou, M. Baruzzo, A. Hakola, et al., Overview of the third JET deuterium-tritium campaign, Plasma Phys. Control. Fusion (2025) http://dx.doi.org/10.1088/1361-6587/adbd75.
[52] C. Giroud, et al., High current Ne-seeded ITER baseline scenario in JET D and D-T, in: 26th International Conference on Plasma Surface Interaction in Controlled Fusion Devices, PSI, Marseille, FR, 2024.
[53] S. Henderson, M. Bernert, S. Brezinsek, et al., Determination of volumetric plasma parameters from spectroscopic N II and N III line ratio measurements in the ASDEX Upgrade divertor, Nucl. Fusion 58 (1) (2017) 016047, http://dx.doi.org/10.1088/1741-4326/aa96be.
[54] A. Huber, M. Wischmeier, S. Wiesen, et al., The radiated power limit in impurity seeded JET-ILW plasmas, Nucl. Mater. Energy 33 (2022) 101299, http://dx.doi.org/10.1016/j.nme.2022.101299.
[55] A. Huber, K. McCormick, P. Andrew, et al., Upgraded bolometer system on JET for improved radiation measurements, Fusion Eng. Des. 82 (5) (2007) 1327–1334, http://dx.doi.org/10.1016/j.fusengdes.2007.03.027, Proceedings of the 24th Symposium on Fusion Technology.
[56] T. Bosman, M. Bernert, L. Ceelen, et al., X-point radiator control and its dynamics in ASDEX Upgrade and JET deuterium–tritium discharges, Nucl. Fusion 65 (1) (2024) 016057, http://dx.doi.org/10.1088/1741-4326/ad99cc.
[57] P. Schneider, C. Angioni, F. Auriemma, et al., Isotope physics of heat and particle transport with tritium in JET-ILW type-I ELMy H-mode plasmas, Nucl. Fusion 63 (11) (2023) 112010, http://dx.doi.org/10.1088/1741-4326/acf560.
[58] L. Frassinetti, C.P. von Thun, B. Chapman-Oplopoiou, et al., Effect of the isotope mass on pedestal structure, transport and stability in D, D/T and T plasmas at similar β_N and gas rate in JET-ILW type I ELMy H-modes, Nucl. Fusion 63 (11) (2023) 112009, http://dx.doi.org/10.1088/1741-4326/acf057.
[59] M. Groth, V. Solokha, S. Aleiferis, et al., Characterisation of divertor detachment onset in JET-ILW hydrogen, deuterium, tritium and deuterium-tritium low-confinement mode plasmas, Nucl. Mater. Energy 34 (2023) 101345, http://dx.doi.org/10.1016/j.nme.2022.101345.
[60] A. Perek, W.A.J. Vijvers, Y. Andrebe, et al., MANTIS: A real-time quantitative multispectral imaging system for fusion plasmas, Rev. Sci. Instrum. 90 (12) (2019) 123514, http://dx.doi.org/10.1063/1.5115569.
[61] M. Komm, I. Khodunov, J. Cavalier, et al., Divertor impurity seeding experiments at the COMPASS tokamak, Nucl. Fusion 59 (10) (2019) 106035, http://dx.doi.org/10.1088/1741-4326/ab34d2.
[62] Y. Feng, M. Jakubowski, R. König, et al., Understanding detachment of the W7-X island divertor, Nucl. Fusion 61 (8) (2021) 086012, http://dx.doi.org/10.1088/1741-4326/ac0772.
[63] Y. Feng, V. Winters, D. Zhang, et al., Conditions and benefits of X-point radiation for the island divertor, Nucl. Fusion 64 (8) 086027, http://dx.doi.org/10.1088/1741-4326/ad5606.
[64] D. Zhang, Y. Gao, Y. Feng, et al., 2D structure of the radiation layer in W7-X and the impact of plasma surface interactions on shaping the profiles, in: 26th International Conference on Plasma Surface Interaction in Controlled Fusion Devices, PSI, Marseille, FR, 2024.
[65] V.R. Winters, F. Reimold, Y. Feng, et al., First experimental confirmation of island SOL geometry effects on detachment in Wendelstein 7-X, Nucl. Fusion 64 (12) (2024) 126047, http://dx.doi.org/10.1088/1741-4326/ad820e.
[66] G. Federici, W. Biel, M. Gilbert, et al., European DEMO design strategy and consequences for materials, Nucl. Fusion 57 (9) (2017) 092002, http://dx.doi.org/10.1088/1741-4326/57/9/092002.
[67] R. Dux, A. Loarte, E. Fable, et al., Transport of tungsten in the H-mode edge transport barrier of ITER, Plasma Phys. Control. Fusion 56 (12) (2014) 124003, http://dx.doi.org/10.1088/0741-3335/56/12/124003.
[68] O. Pan, T. Lunt, M. Bernert, et al., The compact radiative divertor in ASDEX Upgrade and EU-DEMO, experiments and simulations, in: 29th IAEA Fusion Energy Conference, London, UK, 2023.
[69] A. Kallenbach, R. Dux, S. Henderson, et al., Divertor enrichment of recycling impurity species (He, N2, Ne, Ar, Kr) in ASDEX Upgrade H-modes, Nucl. Fusion 64 (5) (2024) 056003, http://dx.doi.org/10.1088/1741-4326/ad3139.
[70] T. Pütterich, E. Fable, R. Dux, et al., Determination of the tolerable impurity concentrations in a fusion reactor using a consistent set of cooling factors, Nucl. Fusion 59 (5) (2019) 056013, http://dx.doi.org/10.1088/1741-4326/ab0384.
[71] M. Bernert, T. Eich, A. Kallenbach, et al., The H-mode density limit in the full tungsten ASDEX Upgrade tokamak, Plasma Phys. Control. Fusion 57 (1) (2014) 014038, http://dx.doi.org/10.1088/0741-3335/57/1/014038.
[72] T. Lunt, M. Bernert, D. Brida, et al., Compact radiative divertor experiments at ASDEX Upgrade and their consequences for a reactor, Phys. Rev. Lett. 130 (2023) 145102, http://dx.doi.org/10.1103/PhysRevLett.130.145102.
[73] R. Pitts, S. Bardin, B. Bazylev, et al., Physics conclusions in support of ITER W divertor monoblock shaping, Nucl. Mater. Energy 12 (2017) 60–74, http://dx.doi.org/10.1016/j.nme.2017.03.005, Proceedings of the 22nd International Conference on Plasma Surface Interactions 2016, 22nd PSI.
[74] R. Wenninger, M. Bernert, T. Eich, et al., DEMO divertor limitations during and in between ELMs, Nucl. Fusion 54 (11) (2014) 114003, http://dx.doi.org/10.1088/0029-5515/54/11/114003.